Medium Energy Concentrator Spectrometer on board the X-ray Astronomy Satellite SAX. Preliminary results of ground X-ray calibrations.

G.Boella, L.Chiappetti, G.Conti, S.Molendi

CNR - Istituto Fisica Cosmica e Tecnologie Relative - Via Bassini 15 - 20133 Milano - Italy

G.Cusumano, S.Del Sordo, G.La Rosa, M.C.Maccarone, S.Re, B.Sacco, M.Tripiciano

CNR - Istituto Fisica Cosmica con Applicazioni all' Informatica - Via Stabile 172 - 90139 Palermo - Italy

H.Brauninger, W.Burkert

Max Planck Institut für Extraterrestrische Physik - D8046 Garching - Germany

ABSTRACT

The scientific instrumentation on board the X-ray Astronomy Satellite SAX includes a Medium Energy Concentrator / Spectrometer (MECS), operating in the energy range 1.3-10 keV, which consists of three identical instruments, each composed by a grazing incidence Mirror Unit with focal length of 1850 mm and by a position sensitive Gas Scintillation Proportional Counter. The MECS flight instruments have been calibrated at the X-ray PANTER facility of the Max Planck Institute and the preliminary results are presented in the paper.

Keywords: X-ray spectrometers, X-ray imaging, X-ray astronomical payloads.

1. INTRODUCTION

The main scientific objectives of the Medium Energy Concentrator / Spectrometer (MECS) on board the X-ray Astronomy Satellite SAX [1][2][3] are:
- broad band spectroscopy (E/ ΔE = 5 - 12) from 1.3 to 10 keV
- imaging with angular resolution at the arcmin level
- study of timing variability of X-ray sources on time scale down to the millisecond.

To reach the desired sensitivity levels with the allowed dimensions of the satellite, the MECS consists of three identical instruments, each composed by a Mirror Unit (MU) with a Xenon filled position sensitive Gas Scintillation Proportional Counter (GSPC) in the focal plane. A fourth identical MU is used for the Low Energy Concentrator / Spectrometer (LECS) in front of the ESA / SSD proportional counter with energy sensitivity extended down to 0.1 keV [4].

1.1. The instrument

The design of the MU was published in a previous paper [5]. Each MU is composed of 30 nested coaxial and confocal mirrors. The mirrors have a double cone geometry to approximate the Wolter I configuration, with diameters ranging from 162 to 68 mm, total length of 300 mm, thickness from 0.4 to 0.2 mm and focal length of 1850 mm. A replica technique by nickel electroforming from super-polished mandrels was used for making the mirrors [6]. A Development Model of the MU was built and tested for X-ray imaging characteristics [7] and then the Engineering Qualification Model [8] and the four Flight Model MUs [9] have been produced and successfully tested for acceptance.

The focal plane detectors are Xenon filled GSPCs (fig. 1), working in the range 1.3 to 10 keV with an energy resolution of ~ 8.0 % at 5.9 keV and a position resolution of ~ 0.5 mm (corresponding to ~ 1 arcmin) at the same energy. The gas cell is composed by a cylindrical ceramic body (96 mm internal diameter) closed at the top by a 50 μm thick entrance Beryllium window with 30 mm diameter and on the bottom by an UV exit window in Suprasil quartz with 80 mm diameter and 5 mm thickness. The input window is externally supported by a Beryllium strongback structure, 0.3 mm thick, which consists of a ring (10 mm inner diameter, 1 mm width) connected to the window border by four ribs. Two Fe^{55} collimated calibration sources, with an emission rate of about 1 count per second, are located, diametrically opposed, near the edge of the Be window. Furthermore a passive ion shield window made of a multilayer of polyamide and aluminium nitrate (Metorex) is placed in front of the detector.

Two grids inside the cell separate the absorption/drift region (20 mm depth) from the scintillation region (17.5 mm depth). The internal top surface around the Be window is metallized with 2 μm of Nickel to allow good uniformity of the electric field in the central region of the cell. The UV readout system consists of a crossed-wires anode position sensitive photomultiplier with a typical quantum efficiency of 20 % at the wavelength produced by the scintillation process (~ 170 nm). The duration of

the light pulse (Burst Length, BL) is used to discriminate genuine X-rays against induced background or events absorbed directly in the scintillation region.

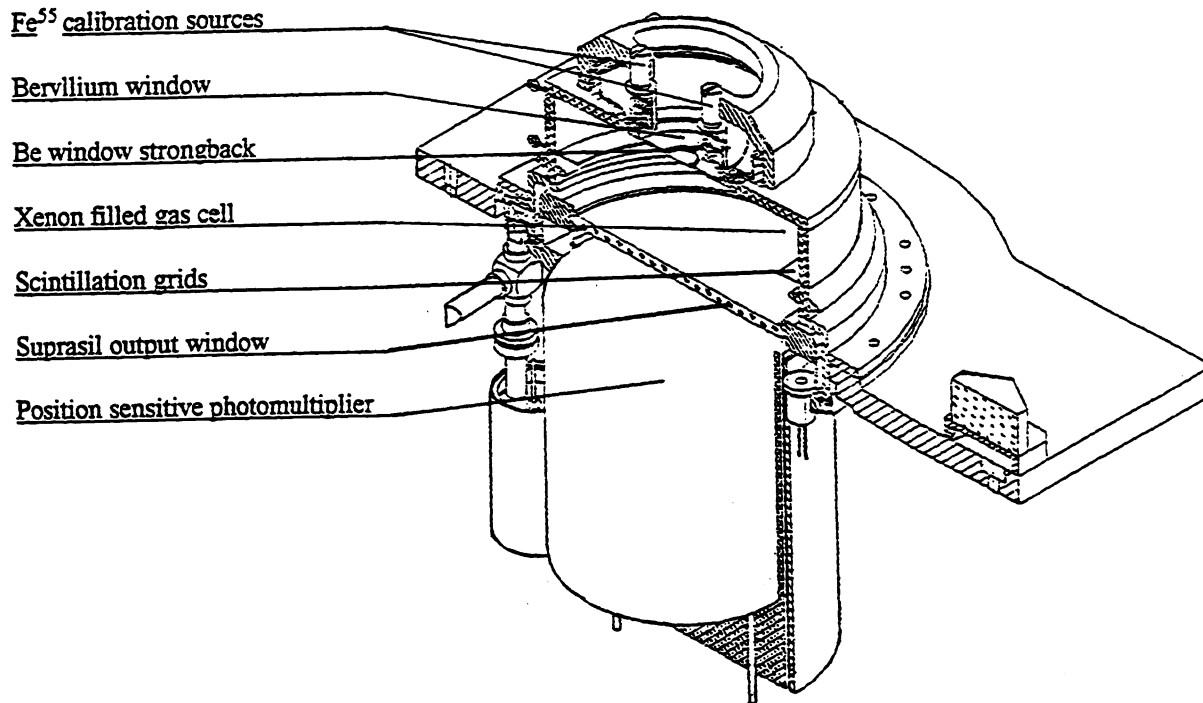A scientific model of the GSPC was tested and the results are published in a previous paper [10].

Fe^{55} calibration sources

Beryllium window

Be window strongback

Xenon filled gas cell

Scintillation grids

Suprasil output window

Position sensitive photomultiplier

fig. 1. Gas Scintillation Proportional Counter.

2. CALIBRATIONS

The three flight MECS instruments, together with the LECS flight unit, were extensively calibrated (about 170 millions photons per detector) at the 130-meter long X-ray PANTER facility of Max Planck Institut für Extraterrestrische Physik in Munich (FRG) [11], during 7 weeks in October, November 1994. During a first run two MECS instruments, hereafter named ME2 and ME3, were calibrated together using two different parts of the 80 cm diameter X-ray beam, and, in the same way, the third MECS instrument (ME1) together with the LECS [12] were measured during a second run.

2.1. Experimental set-up

The experimental set-up is shown in fig. 2: the Mirror Units were mounted on an optical bench which allowed, via remotely controlled manipulators, a linear translation (T1) and two rotations (R1 and R2); furthermore one of the two MUs could be manually rotated (R3 and R4) during the initial alignment, to take into account the divergence of the two parts of the beam. The detectors were fixed to a separate optical bench with three linear manipulators (T2, T3 and T4) and one of the two could be manually translated along T5 and T6 for initial alignment. Moreover, the whole assembly MUs-detectors were mounted on a great table that could be remotely rotated (R5 and R6) for off-axis measurements. The resolution of the linear manipulator encoders is 1.25 μm/step while the rotation manipulator encoders R5 and R6 have a resolution of 761 steps/arcmin and 14430 steps/arcmin respectively.

The translation manipulator T1 could position in front of the detectors alternatively the two MUs or two 40 mm diameter holes for direct beam measurements (so called flat-fields), or two multipinhole masks with a square matrix of 121 holes (0.561 ± 0.007 mm diameter) with 4 mm pitch. The apertures and the masks (not shown in fig. 2) were located on the screen behind the MUs.
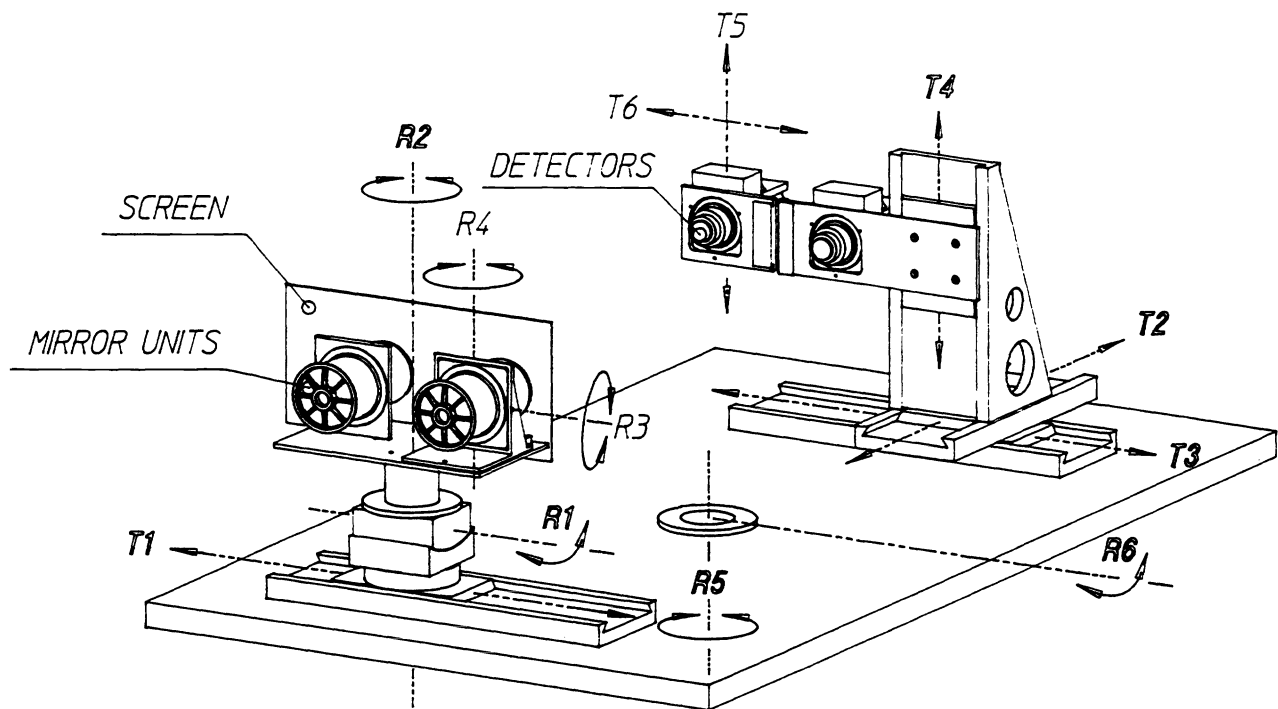
fig. 2.   Ground calibrations experimental set-up.

Two interchangeable X-ray sources are available at the PANTER facility: the first one directly installed in vacuum for energy lines up to 3 keV [13] and a second one for higher energies, separated from the vacuum by a Beryllium window. The high voltage supply and emission current of the X-ray sources and the filter wheels (16 positions) can be remotely controlled and were adjusted to obtain for each measure type the desired counting rate and the more convenient energy spectrum. An independent proportional counter, placed at the entrance of the test chamber, is used to monitor the X-ray beam intensity (Monitor Counter). The data related to the experimental conditions, i.e. time, X-ray source voltage and current set-up, manipulator encoder outputs and monitor counter rate, are continuously recorded and stored in housekeeping (HK) files that have been off-line correlated to the measure runs.

The instrument Electronic Unit (EU; common to all three detectors) was connected to a Test Equipment (TE) including a bus probe emulating the satellite OBDH bus. Data acquisition (in the form of telemetry packets) and instrument control was performed via a Vaxstation controlling the TE, and connected on a Local Area Network (LAN). To this LAN were attached a further Vaxstation for intermediate storage, two PCs for Quick Look, and one PC for data archiving onto magneto-optical disk (for later off-line analysis at home; PANTER HK data were transferred daily via Wide Area Network). The instrument EU performed very well and supported source rates up to 4000 cts/s beyond the specification of 2000 cts/s.

The initial MUs and detectors alignment (within few arcmin) was performed with a divergent He-Ne laser beam that simulates the X-ray beam: the MUs were aligned (R1, R2, R3 and R4) looking at the shape of the out of focus images of the laser point like source; then the focalized spots were centred (T3, T4, T5 and T6) in the middle of the detector Beryllium windows. The final adjustment (within 15 arcsec) was done at X-ray wavelength (1.5 keV), using the photons that, as a consequence of the finite distance of the source, are reflected only by the first cone of all the mirrors of the MUs; these photons must form a symmetrical and uniform ring at the border of the detector (30 mm diameter). We have verified that this very simple and quick method is sufficient to obtain the desired accuracy for the MECS and LECS calibrations. The best focus position was found at 1.5 keV, using the manipulator T2, by minimising the Half Power Radius of the acquired images.

The measurements were made at 0.92 keV (Cu-Lα), 1.25 keV (Mg-Kα), 1.48 keV (Al-Lα), 1.74 keV (Si-Kα), 2.02 keV (P-Kα), 3.12 keV (Ag-Lα), 4.52 keV (Ti-Kα), 5.44 keV (Cr-Kα), 6.44 keV (Fe-Kα), 7.52 keV (Ni-Kα), and 8.1 keV (Cu-Kα). For each energy line three main measure types were done: MUs (on-axis and off-axis), flat-fields and multipinhole scans; a typical MU acquisition run contains half a million events. All such measurements were performed at the nominal instrument setting. Additional measurements (not yet analysed) were performed in non-nominal conditions (detector High Voltages, count rate).

3. DATA ANALYSIS AND RESULTS

In what follows the main results of the calibration analysis are presented, considering a sample of the data (e.g. limiting to one detector or to a subset of the runs). The analysis of the complete set is in progress.

3.1. Spectral resolution

For this analysis data from on-axis MUs runs have been used, to minimise any dependence of the detector gain from the position (see 3.2). For each calibration source line (from 1.25 to 8.1 keV) the energy spectra have been accumulated with a Burst Length selection in order to reject events converting in the scintillation region (events with short BL) or double events (long BL). In particular, the photons that convert in the scintillation region are detected with an incorrect energy, due to the shorter UV-light bursts.

Fig. 3 shows a typical energy spectrum. Generally a good fit can be obtained using a single gaussian curve but in some cases (for example for the Titanium line) there is evidence of a second, weaker line (in this case the Kβ Titanium line). A good fit is than obtained using two gaussian curves of different amplitudes (see fig. 4). For low energy spectra the presence of a high background, mainly due to Bremsstrahlung from the X-ray source, makes it more difficult to obtain a good fit with gaussian curves only. A more detailed model will be used to compute gain and energy resolution for the low energy cases as soon as we complete the preliminary analysis for the three detector units.

From fig. 3 is also evident the presence of the fluorescent photons (in this case around channel 30). This well known effect [14][15], consists in the escape from the detector gas cell of X-ray photons generated by the rearrangement of the Xenon atoms after the absorption of the incident X-ray (this effect is present only for energies greater than 4.782 keV i.e. the Xenon L edge). In fact, after the ejection of the photo-electron, the Xenon atom remains in an excited state and may relax with the emission of another (Auger) electron or with the emission of a fluorescence photon of a given energy.

This photon may or may not be reabsorbed inside the detector gas cell. If the fluorescent photon leaves the detector the energy deposited is :

$$E_{residual} = E_{incident} - E_{fluorescent\ photon}$$

This escape fraction can be estimated from combined energy-BL spectra and is in good agreement, for relative intensities and energy values, with the result of a numerical model of the Xe detector .
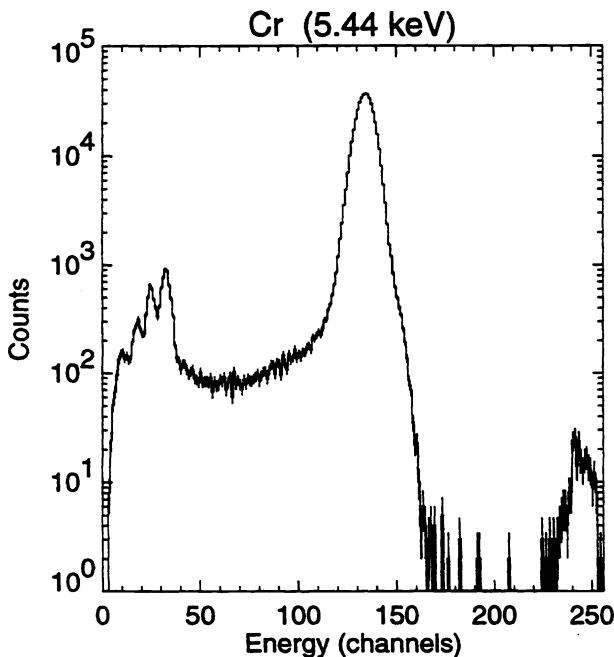

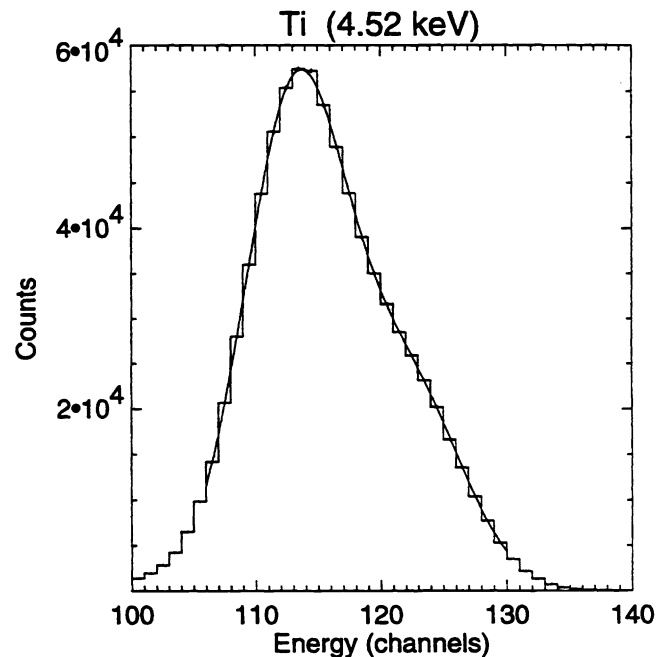fig. 3.   Energy spectrum of Cr line.

fig. 4.   Energy spectrum of Ti line.

3.2. Gain

The results of the gain analysis are reported, for ME3, in fig. 5 as detector gain vs. energy. The discontinuity at 4.780 keV (the jump in the detector gain) is due to the Xenon L absorption edge caused by a decrease in the photon-electron conversion efficiency of the gas. This effect was also found in the Exosat and Tenma GSPC detectors [16]. The solid straight lines in fig. 5 correspond to the best fit of the experimental points on each side of the edge (Mg, Al, Si, P, Ag and Ti lines for the left side, and Cr, Fe and Cu lines for the right side). The analytical results of the fits are:

$$Gain\ (channel)\ =\ 23.49*E\ (keV)\ -\ 0.089 \quad \text{before the discontinuity}$$
$$Gain\ (channel)\ =\ 23.49*E\ (keV)\ -\ 1.413 \quad \text{after the discontinuity}$$

The spectral analysis allows also to derive the spectral resolution of the detector as a function of energy. The sigma of gaussian fits to each line are found to be in good agreement with the theoretical prediction: $\sigma\ (channels)\ =\ A*E^{1/2}$ where the best fit of the experimental points gives $A\ =\ 1.90$. Given that $FWHM\ (channels)\ =\ \sigma\ /\ 0.425$, and using the gain relation derived above, it is possible to plot in fig. 6 the resolution in the more usual form of $\Delta E\ /\ E\ (FWHM\ \%)$.
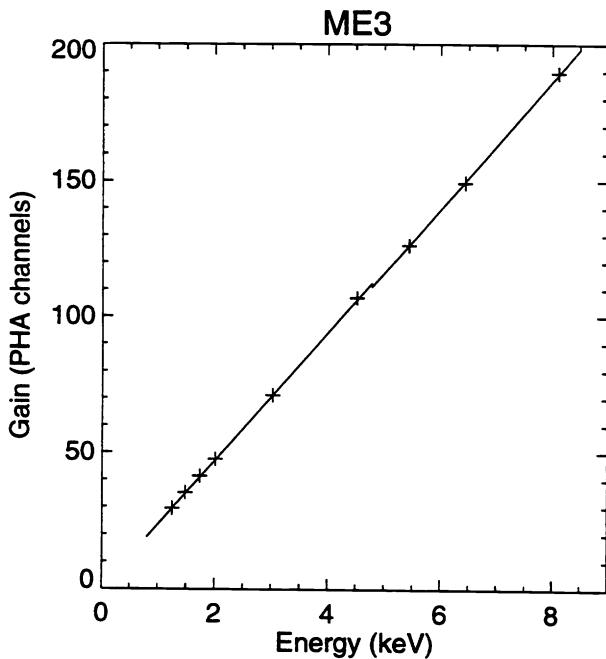

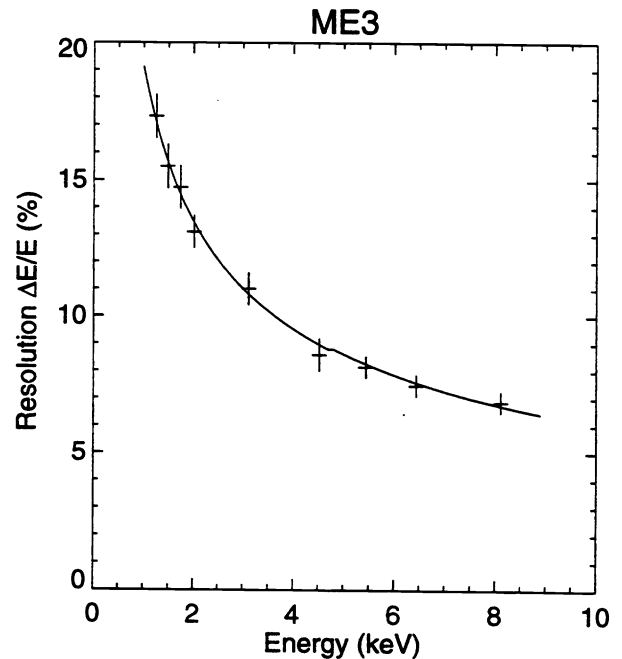fig. 5.   ME3: gain vs. energy.

fig. 6.   ME3: energy resolution.

A dependency of the gain on the position is present in all three detectors (in the sense that a photon falling at the edge of the detector will be revealed in a different channel than a photon falling close to the centre), and can be calibrated analysing individual spectra of each spot of the multipinhole measurements (see also 3.5).

The core of the line in each spectrum has been fitted with a gaussian, and the peak position in channels has been associated with the spot position in pixels, obtaining a set of sparse values $G_i\ =\ G(x_i,\ y_i)$. For each run a gain map has been derived with a biquadratic interpolation of the above values on each pixel within the detector window. The values have been normalized to the gain at the detector centre, obtaining a relative gain map $g(x,\ y)\ =\ G(x,\ y)\ /\ G(x_0,\ y_0)$.

It has been found that the relative gain is extremely stable with energy, as well as unaffected by temporal variations of the absolute gain (this is not surprising since the spatial dependency of gain is due to geometrical disuniformities in the PMT anodes and/or entrance window), therefore the gain maps of all runs at all energies can be averaged to produce a single gain map per detector, with a high accuracy.

The relative gain maps are shown in fig. 7. The range of the relative gain (assuming 1.00 in the detector centre) is 0.90-1.10 for ME1, 0.99-1.06 for ME2 and 0.96-1.03 for ME3, with an rms error < 0.002 on almost all the field of view.

The absolute gain can be monitored continuously using the built-in Fe[55] calibration sources and compensated. It has been found that there is a long term exponential trend (with a decay of several hours) when the instruments are switched on after a long period of inactivity, attributed to time constants in the power system.

There is also a weak dependency on count rate (in the sense that the gain is depressed for the lowest count rates, typically during the flat-field measurements), provisionally attributed to time constants in the EU baseline restorer. Investigation of this effect is in progress.
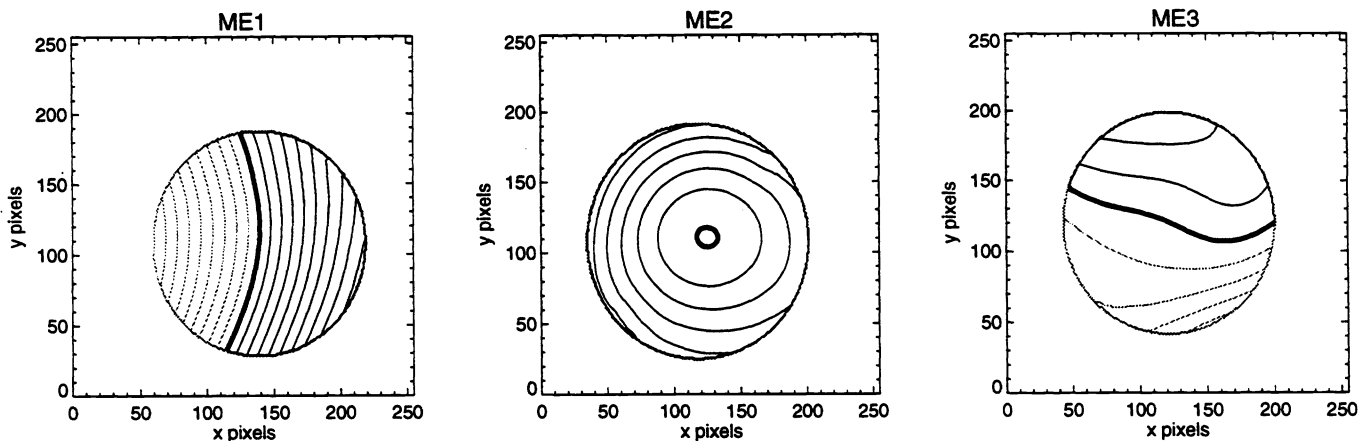

fig. 7. Relative gain maps (gain as percentage of the value at detector centre). Thick lines indicate a gain of 1.00. Contours are spaced by 0.01. Contours lower than 1.00 are in lighter shade. See text for ranges.

3.3. Absolute efficiency

The detector absolute efficiency is mainly determined by the X-ray transparency of the detector Beryllium window and of the Metorex passive ion shield window and by the gas cell conversion efficiency. All these quantities depend obviously from the incident photon energy.

The transmission coefficient of the windows comes from:

$$T_w = exp(-\mu(E) * x)$$

where $\mu(E)$ is the absorption coefficient of the material for the energy E and x is the window thickness. To compute the gas cell absorption probability P_a one can us the relation:

$$P_a = 1 - exp(-\mu_X(E) * D)$$

where $\mu_X(E)$ is the Xenon absorption coefficient for the energy E and D is the detector drift region depth. In the computation of the gas cell photon absorption probability we consider only the drift region depth because the events that convert in the scintillation region are rejected to improve the energy resolution of the detector. The absolute efficiency of the detector is given by
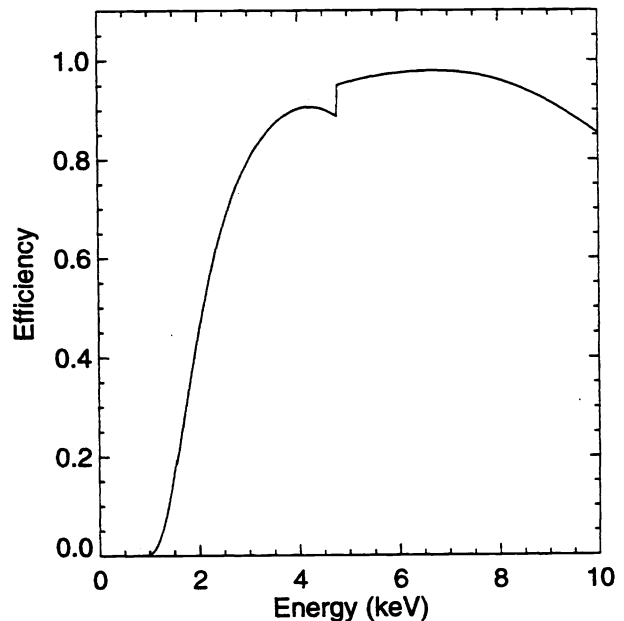
$$\varepsilon = T_w(E) * P_a(E)$$

fig. 8. Theoretical detector absolute efficiency

and is shown in fig. 8 as a function of the incident photon energy. The low energy part of the curve (0 - 3 keV) is dominated by the transmission coefficient of the two windows, while the high energy part (E > 7 Kev) is dominated by the conversion efficiency of the gas. The characteristic feature at 4.78 Kev is due to a sudden increase in the Xenon photoelectric cross section caused by the L-shell activation.

3.4. Mirror Units effective area

The on-axis effective area A_e is defined as:

$$A_e = (N_{out}/N_{in}) * A_{MU}$$

where N_{in} is the number of the arrival photons on the MU, N_{out} is the number of photons that reach the focal plane, and A_{MU} is the geometrical area of the MU, which is about 105 cm² for a parallel beam. In the case of a source at finite distance (divergent beam of the PANTER facility), this value must be reduced to about 102 cm² for the above mentioned direct reflection from a small part of the surface of each mirror.

N_{out} is obtained from the total number of counts, N_{MU} detected with the MU on-axis, during an integration time T_1, and corrected for the dead time and for the detector efficiency (with MU) ε_{MU}:

$$N_{out} = N_{MU}/\varepsilon_{MU}$$

N_{in} is obtained by the total number of counts N_{FF}, detected during a flat-field exposure in the time interval T_2, corrected for the dead time and for the detector efficiency (for flat-field) ε_{FF} and normalized to the geometrical areas and to the integration times:

$$N_{in} = (N_{FF}/\varepsilon_{FF}) * (T_1/T_2) * (A_{MU}/A_{DET}) * K$$

where A_{DET} is the geometrical area of the detector, and K is a correction factor taking into account the different flux, on detector and on mirrors unit, due to their different distance from the PANTER source.
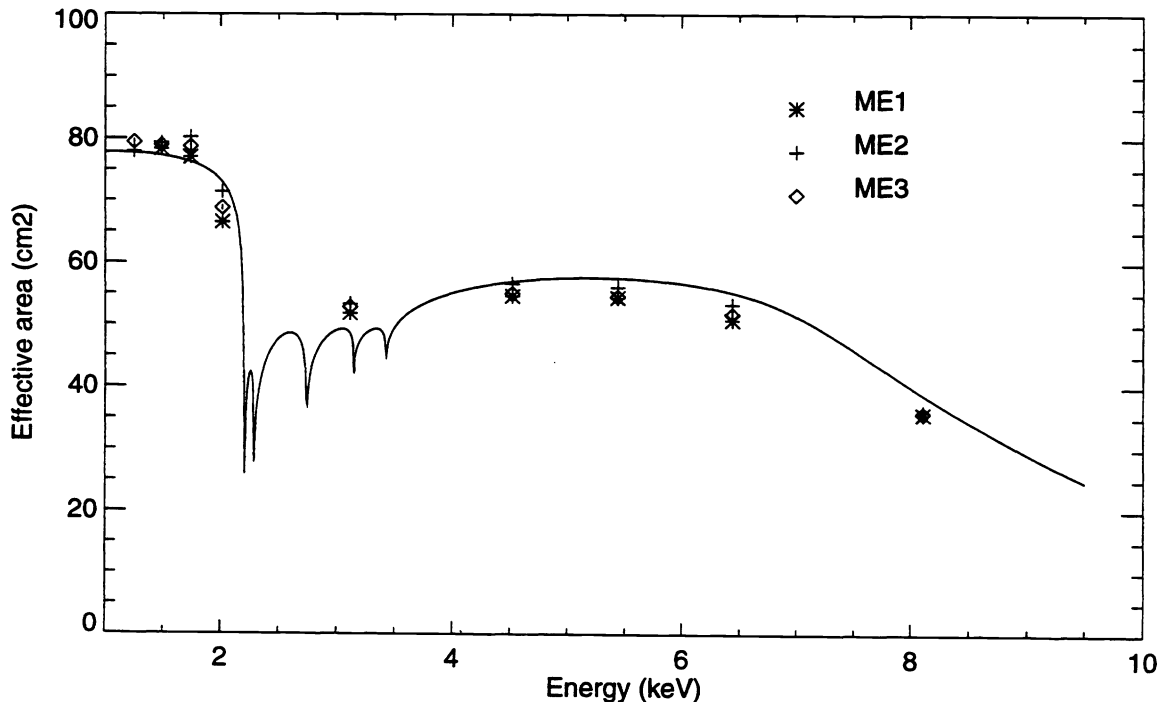

fig.9 Mirror Units effective area

The Be window strongback structure has a strong influence on the detector efficiency. For MU measurements, the detector efficiency is determined by the transparency of the 50 μm thick window in its central region while, in the flat-field measurements, photons are uniformly distributed on the entire window and therefore the strongback structure must be taken into account. The difference between the two values ε_{MU} and ε_{FF} is mainly evident at low energies.

The events accumulated during MU and flat-field measurements have been corrected for the instrumental background and have been selected in the same energy range around the central value of the line. Events from the entire detector, in this energy range, have been considered, apart the ones located in two small areas around the calibration sources.

Fig. 9 shows the on-axis effective area vs. energy. The theoretical behaviour, as derived by ray-tracing simulation of a point source located at the same distance as the X-ray PANTER source, fits the experimental data only with the introduction of a constant factor of 0.925; the result of the fit is represented by the solid line in fig. 9. Extrapolation to infinite distance requires an increment of ~ 2% of all previous values. Except the 3 keV silver line, data agree well with the theoretical prediction. The high efficiency at 3 keV has been also measured in previous X-ray tests [9]. A possible explanation of this effect could be the presence, on the reflecting surfaces of the optics, of a thin contamination hydrocarbon film which enhances the X-ray reflectance mainly in the 2 ÷ 4 keV region where gold M-edges are present [17]. This effect should be time-dependent; an accurate in-flight calibration is therefore necessary. The derived effective areas of the MU are also in good agreement with the effective areas measured on the same units during the acceptance tests [9].

3.5. Geometric distortions

The position response of the detector is affected by some nonlinearities which come from three main contributions: the first derive from spatial disuniformities in the PMT gain. The second one is due to a geometrical effect, i.e. different scintillation positions are seen by the PMT under different solid angles leading to a variation in light collection and then to an error in evaluating the position of the scintillation event; these effects are not energy dependent. The third contribution is related to the distortion of the electric field near the Be window, due to a slight curvature of the window itself. This effect is more enhanced at low energy because of the shorter mean penetration depth of low energy photons (0.4 mm being the mean penetration depth of 1.5 keV photons with 1 atm of Xe), that produce a paraxial shift of the scintillation point with respect to the point in which the X-ray photoabsorption occurs.

In order to correct for this effects the multipinhole measurement runs have been considered; for each energy at least one measurement has been done and, in some cases, a scan has been performed, shifting the mask with steps of 1 mm, so to have a fine coverage of the detector sensitive area with a grid of 1 x 1 mm.

A preliminary verification has been made that the detector electronic axes are aligned with the detector geometrical axes (determined by the strongback ribs), using the flat-field measurements at low energies, where the shadow by the window strongback is clearly visible. This allowed to correct for a slight ($\leq 1°$) rotation between multipinhole masks and detectors.

The barycentres (in pixels) of the spot images generated by the multipinhole mask, placed 1690 mm far from the detector, are calculated with a bidimensional gaussian fit. Then, taking into account the real pitch of the holes as projected onto the Be window, a transformation law has been derived to convert the coordinates from pixels to millimetres. The transformation law that best fits the position in millimetres of the holes is a second degree polynomial, with a dependence on the energy only in the first degree term:

$$X = A_3 * (K_x - A_1)^2 + A_4 * (1 + A_5/E) * (K_x - A_1)$$

$$Y = A_6 * (K_y - A_2)^2 + A_7 * (1 + A_8/E) * (K_y - A_2)$$

where K_x and K_y are the original coordinates in pixels, E is the energy in keV, X and Y are the new coordinates (expressed in mm) and A_n are the best fit parameters.

The plate scale of the three detectors is of the order of 0.17 mm/pixel. A small anisotropy in the linear coefficients A_4 and A_7 is present between x and y axes, in particular this value is about 5 % for ME1, while is negligible (less than 1 %) for ME2 and ME3. This transformation law reconstructs the position of the holes with a rms error of 80 μm in a central region of 6 mm radius and 120 μm in the whole detector. To improve these results a reconstruction law with a third order term will be derived. Also a different approach is under evaluation, that is a correction of the geometrical distortions on the basis of an x-y correction map.

3.6. Point Spread Function

The Point Spread Function (PSF) of the MECS is the convolution of the MU PSF with the detector PSF. The latter is expected to be a gaussian with $\sigma \propto E^{-1/2}$.

The multipinhole runs have been used to measure the detector PSF; the data are in good agreement with the theoretical prediction for E < 4 keV, while for E > 4 keV the σ appears to be larger than expected. The disagreement between data and model is due to the fact that at high energies the size of the PSF becomes comparable to the size of the holes, making the pinhole approximation no longer valid. In principle the σ of the detector PSF, at high energies, could be recovered by fitting the convolution of the emission from a hole of finite size with a gaussian, to the data. In practice it can be more conveniently derived from the flat field data, by fitting the radial profile of the detector edges with the convolution of a gaussian with a step function.

The MU PSF, for which a set of measurements has already been obtained during previous calibration runs [9], is characterized by broad low surface brightness wings.

The preliminary analysis of the MECS PSF has been restricted in three ways: 1) by considering only the on-axis PSF, 2) by assuming only a radial dependence of the PSF and 3) by using only data from the ME3 instrument.

The adopted PSF model is the sum of 2 components: a gaussian $G(r)$, and a generalized lorentzian, $L(r)$:

$$G(r) = c_g * exp \, (-r^2/2\sigma^2) \qquad\qquad L(r) = c_l * [\, 1 + \, (r/r_l)^2 \,]^{-m}$$

where r is the distance from the peak of the emission and c_g, c_l, σ, r_l and m are the parameters of the model which have been derived by fitting the radial profiles accumulated from the calibration data at the energy lines of Mg, Al, Si, P, Ag, Ti Cr, Fe and Cu. Fig 10 shows, as an example, the fit to Al data.

By imposing that the integral of the PSF over the entire plane be equal to unity,

$$2\pi \int_0^\infty PSF(r) \, r \, dr \equiv 1$$

the number of independent parameters are reduced to 4: σ, r_l, m and R, where $R = c_g / c_l$.
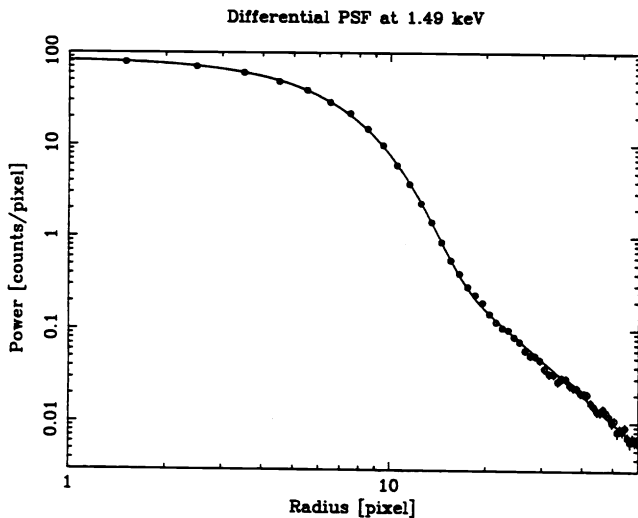

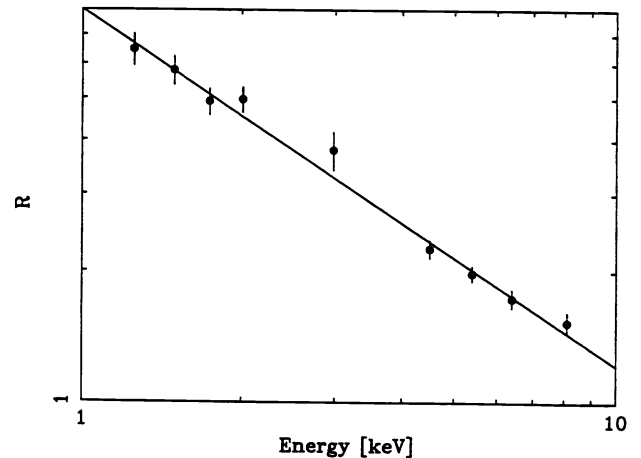fig. 10. ME3: differential PSF at 1.49 keV.

fig. 11. ME3: The R parameter, defined as c_g / c_l, as function of energy.

The dependency of these 4 parameters from the energy has been reproduced through simple algebraic functions. Fig 11 shows, as an example, the fit of the values derived, at the 9 calibration energies, for the parameter R.

The complete analytical expression for the PSF reads:

$$PSF(r,E) = \frac{1}{2\pi\left[R(E)\sigma^2(E) + \frac{r_l^2(E)}{2(m(E)-1)}\right]}\left\{R(E)\exp\left(-\frac{r^2}{2\sigma^2(E)}\right) + \left[1 + \left(\frac{r}{r_l(E)}\right)^2\right]^{-m(E)}\right\} \qquad (1)$$

where $R(E)$, $\sigma(E)$, $r_l(E)$ and $m(E)$ are algebraic functions of E.

Since both $G(r)$ and $L(r)$ can be analytically integrated in rdr, equation (1) can be used to derive an analytical expression for the Integral Point Spread Function (IPSF), which is defined as:

$$IPSF(\rho) = 2\pi\int_0^\rho PSF(r)\, r\, dr \qquad (2)$$

Equation (2) has been used to evaluate, for ME3, the 50 % and 80 % Power Radius (PR) at three different energies and the obtained values are reported in table 1 (ME1 and ME2 give PR values very close to the ME3 ones).

E (keV)	50 % PR (arcsec)	80 % PR (arcsec)
1.48	105	165
6.44	75	150
8.1	75	150

table 1. ME3: 50 % and 80 % Power Radius at three energies.

ACKNOWLEDGEMENTS

REFERENCES

(1)   L.Scarsi, "The SAX mission", *Adv. Space Res. 3, 491* (1984).

(2)   G.Spada, "SAX Scientific Instrumentation", *Proc. Conference on "Non thermal and Very High Temperature Phenomena in X-ray Astronomy", 217*, Roma (1983).

(3)   C.Perola, "The Scientific Objectives of the SAX Mission", *Proc. Conference on "Non thermal and Very High Temperature Phenomena in X-ray Astronomy", 173*, Roma (1983).

(4)   A.N.Parmar, A.Smith, and M.Bavdaz, "A Low Energy Gas Scintillation Proportional Counter for the SAX X-ray Astronomy Satellite", *IAU Coll. 123 on "Observatoires in Earth Orbit and Beyond", 457* (1990).

(5)   O.Citterio, G.Conti, E.Mattaini, B.Sacco and E.Santambrogio, "Optics for X-ray Concentrators on Board the Astronomy Satellite SAX", *Proc. SPIE 597, 102* (1985).

(6)   O.Citterio, G.Bonelli, G.Conti, E.Mattaini, E.Santambrogio, B.Sacco, E.Lanzara, H.Brauninger and W.Burkert, "Optics for the X-ray Imaging Concentrators Aboard the X-ray Astronomy Satellite SAX", *Appl. Opt. 27, 1470* (1988)

(7)   O.Citterio, P.Conconi, G.Conti, E.Mattaini, E.Santambrogio, G.Cusumano, B.Sacco, H.Brauninger and W.Burkert, "Imaging Characteristics of the Development Model of the SAX X-ray Imaging Concentrator", *Proc. SPIE 1343, 145* (1990).

(8) G.Conti, E.Mattaini, E.Santambrogio, B.Sacco, G.Cusumano, O.Citterio, H.Brauninger and W.Burkert, "Engineering Qualification Model of the SAX X-ray Mirror Unit. Technical data and X-ray Imaging Characteristics", *Proc. SPIE 2011, 118* (1993).

(9) G.Conti, E.Mattaini, E.Santambrogio, B.Sacco, G.Cusumano, O.Citterio, H.Brauninger, and W.Burkert, "X-ray characteristics of SAX flight mirror units", *Proc SPIE 2279, 101* (1994).

(10) A.Bonura, S.Giarrusso, L.Lombardo, G.Manzo, S.Re, G.LaRosa, F.Celi, R.DiRaffaele, G.Conti, H.Brauninger, and W.Burkert, "Performance characteristics of the Scientific Model of the Medium Energy Concentrator Spectrometer on board the X-ray Astronomy Satellite SAX", *Proc.SPIE 1743, 510* (1992).

(11) B.Aschenbach, H.Brauninger, K.H.Stephan and J.Trümper, "X-Ray Test Facilities at Max Planck Institute, Garching", *Proc. SPIE 184, 234* (1979).

(12) D.D.Martin, M.Bavdaz, A.J.Peacock, and A.N.Parmar, "SAX low-enegy gas scintillation proportional counter (LE-GSPC) calibration and system performance", *these proceedings*.

(13) K.H.Stephan, P.Predhel, B.Aschenbach, H.Brauninger and A.Ondrusch, "Soft X-ray Source for the Max Planck Institute (MPI) Long Beam (130 m) Test Facility", *Proc. SPIE 316, 203* (1981).

(14) F.P.Santos, T.H.V.T.Dias, A.D.Stauffer and C.A.N.Conde, "Variation of energy linearity and w value in gaseous Xenon radiation detectors for X-ray in the 0.1 to 25 keV energy range", *NIM A307, 347* (1991).

(15) J.M.F.Des Santos, C.A.N.Conde and A.C.S.S.M.Bento "The energy linearity of gaseous Xenon radiation detectors for X-rays with energies between 2 and 60 keV: Experimental results", *NIM A324, 611* (1993).

(16) N.E.White, "GSPC calibrations", *EXOSAT Express 11, 51* (1985) *and references therein.*

(17) R.F.Elsner, S.L.O'Dell, and M.C.Weisskopf, "Molecular contamination and the calibration of AXAF", *Proc.SPIE 1742, 6,* (1993).